Phase-Vortex Removal for Quantitative X-Ray Nanotomography with Near-Field Ptychography

Irene Zanette,[1,2,*] Richard Clare,[2,3] David Eastwood,[4,5] Charan Venkata ,[6,7] Franz Pfeiffer,[2]
Peter Cloetens,[8] and Pierre Thibault[1,6,9]

[1]*Department of Physics and Astronomy, University of Southampton, Southampton SO17 1BJ, United Kingdom*

[2]*Chair of Biomedical Physics, Department of Physics and Munich School of BioEngineering, Technical University of Munich, Garching 85748, Germany*

[3]*Department of Electrical and Computer Engineering, University of Canterbury, Christchurch 8020, New Zealand*

[4]*School of Mechanical, Aerospace and Civil Engineering, The University of Manchester, Manchester M13 9PL, United Kingdom*

[5]*University of Manchester at Harwell, Harwell Campus, Didcot, Oxfordshire OX11 0FA, United Kingdom*

[6]*Diamond Light Source, Harwell Science and Innovation Campus, Didcot OX11 0DE, United Kingdom*

[7]*Department of Physics and Astronomy, University College London, London WC1E 6BT, United Kingdom*

[8]*European Synchrotron Radiation Facility, Grenoble 38043, France*

[9]*Department of Physics, University of Trieste, Trieste 34123, Italy*

X-ray ptychotomography in the near-field regime is a promising technique for high-resolution, quantitative, and nondestructive investigations in materials science, paleontology, and biomedicine. X-ray near-field ptychography has been previously demonstrated in projection and tomography mode, but the quantitativeness of the reconstructed data has never been discussed in detail. Here, we use measurements of a sample made of aluminum and nickel microparticles to evaluate the quantitativeness of the volumetric mass-density data. Moreover, we propose an algorithm (VortRem) for the removal of phase vortexes, a type of artifact that frequently occurs in holographic methods. VortRem and the results presented here may be fundamental for extending the applicability of this emerging technique to quantitative three-dimensional characterization studies of light as well as dense samples down to the nanoscale.

I. INTRODUCTION

Three-dimensional (3D) quantitative characterization of samples at submicrometer resolution plays an important role in various disciplines such as nanotechnology, medicine, paleontology, and the life sciences. Yet achieving high-fidelity quantitative nanotomographic data remains a challenging task.

As opposed to other methods [1–4], lens-less phase imaging with hard x rays offers the necessary penetration depth, resolution, and sensitivity to obtain 3D mass-density mapping at the nanometer scale.

Standard far-field ptychography is a robust and well established quantitative technique based on the collection, for each projection, of numerous far-field diffraction patterns from localized areas in the sample [5–7]. It has found important applications in several fields, from hard-tissue biological imaging [8] to integrated circuits [9] and carbon-fiber characterization [10], among the most recent publications. The resolution depends on the scattering properties of the sample and can now reach better than 20 nm in three dimensions [9]. However, the tomographic scan time still reaches several hours, as tens of thousands of diffraction patterns need to be collected. This also limits the maximum size of the sample that can be imaged with far-field ptychography.

Tomography from hard-x-ray holograms (holotomography) yields 3D data of high quality in much shorter times [11–13] and allows for the spatial resolution and the field of view to be tuned depending on the experimental needs. Compared to far-field ptychography, the spatial resolution is typically lower but holotomography is less affected by the finite dynamic range of x-ray detectors. The main limitations of holotomography come from the assumptions used for phase retrieval, which in general cause a loss of the quantitative information. Moreover, the image quality might be affected by background inhomogeneities and strong density variations in the sample [14].

Recently, near-field ptychographic methods have been developed in which a ptychographic reconstruction

---

*[*]irene.zanette@soton.ac.uk

algorithm is adapted to data collected in the holographic regime [15,16]. Near-field ptychography merges the advantages of far-field ptychography and holotomography, as it combines a tunable field of view and relatively short scan times together with direct density measurements as well as the possibility to fully decouple the incident beam from the transmission function of the sample. While "longitudinal near-field tomography" necessitates measurements at different transverse and longitudinal positions of the sample [16], the method used for this experiment and introduced in Ref. [15] only requires scanning of the sample orthogonally to the x-ray beam direction.

In previous experiments, the potential of near-field ptychography has been demonstrated on projections of materials-science specimens [17] and subsequently extended to three dimensions [18,19]. Phase vortexes have been described for projection data of optically thick specimens (see Ref. [15]) and are known to affect the quantitativeness of the results. However, a correction to this type of artifact, which also occurs in other holographic methods, has never been proposed. Furthermore, the quantitative character of the phase measurements obtained with near-field ptychography on reference materials has never been discussed.

In this work, we use near-field ptychographic measurements on a microparticle sample made of known materials to present an algorithm for phase-vortex removal and study the quantitativeness and sensitivity of the phase data obtained with near-field ptychography.

II. THE EXPERIMENT

The phantom sample used for this experiment is made by particles of Al (99% purity) and Ni (99.5+% purity) contained in a glass capillary. The smaller aperture of the capillary has diameter 20 μm. The nominal maximum size of the particles is 15 μm and 45 μm for Al and Ni, respectively [20]. This object resembles samples of materials used for a variety of purposes, including energy storage or catalyst research.

The experiment is performed at the ID16A beam line of the European Synchrotron Radiation Facility in Grenoble, France, at 185 m from the undulator source. The x rays, with a photon energy of 17.05 keV, are focused upstream of the sample by Kirkpatrick-Baez mirrors on a spot of size approximately 20(h)$\times$40(v) nm^2. The distance of the detector from the focal spot is 0.337 m and the sample is located 20.2 mm downstream of the spot. The high-resolution detector with a 0.8448-μm pixel size is lens coupled to a FreLoN CCD camera with 2048 $\times$ 2048 pixels. Considering the geometrical magnification of 16.66, the pixel size at the sample plane is 50.7 nm.

During the ptychography scan, 17 diffraction patterns are captured [21] in the plane perpendicular to the optical axis (see Fig. 1). The exposure time per frame is 0.5 s, while the acquisition time for the ptychographic scan is less than 2 min. An example of one of these holograms is shown in Fig. 1. In total, 800 ptychography scans are performed for different and evenly spaced angular orientations of the sample over 180°. The precision of the rotation
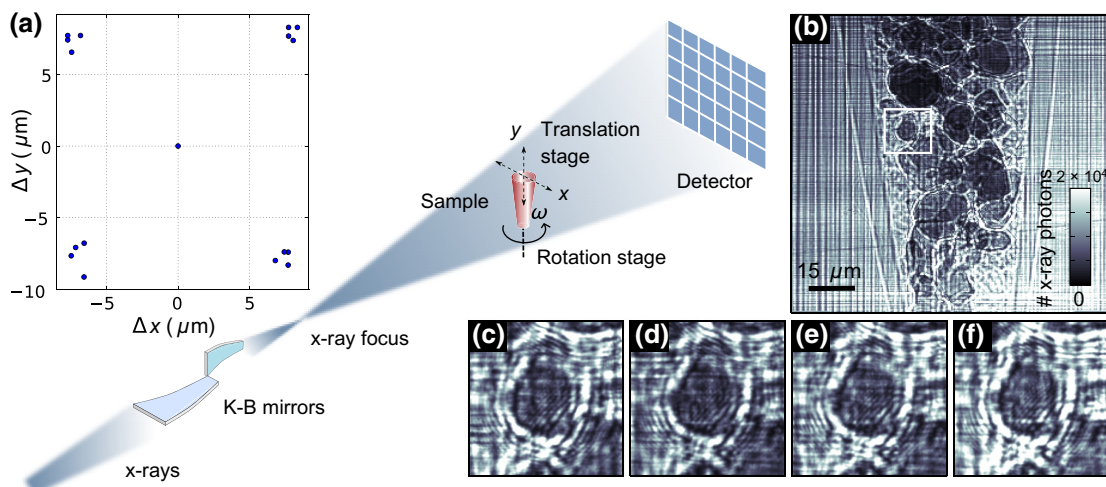

FIG. 1.   A schematic representation of the setup used for near-field ptychography. (a) The scanning pattern used for each projection. (b) A hologram of Al and Ni particles in the glass capillary. The horizontal and vertical stripes in the image are caused by wavefront variation produced by the multilayer-coated Kirkpatrick-Baez mirrors. (c)–(f) The same sample detail at different scan positions [regions of interest (ROIs) of 300 $\times$ 300 pixels], where the displacement of the sample image with respect to the background features can be appreciated. The nonhomogeneous background combined with the scanning procedure provides the necessary information to reconstruct the transmission function of the sample and the illuminating wave front.
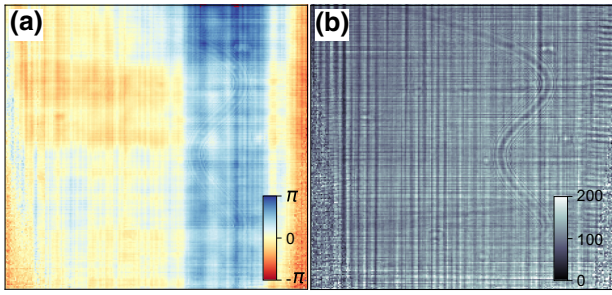
FIG. 2. The (a) phase (in radians) and (b) amplitude (in arbitrary units) of the illumination function retrieved with the near-field ptychographic algorithm. The features of the mirrors used for focusing the beam are clearly visible in both images.

stage used for tomography corresponds to approximately 0.2% of a pixel.

III. DATA ANALYSIS

Prior to the ptychographic reconstructions, the raw images are corrected for geometric distortions introduced by the detector and deconvolved with the theoretical point-spread function of the detector. The analog-to-digital detector units are also converted into the number of x-ray photons in each pixel. For each projection angle, a cross-correlation algorithm is applied to the set of raw images to retrieve the exact displacements of the sample during the ptychographic scan.

Each ptychographic data set is reconstructed independently, using an early version of the PTYPY software [22]. An initial reconstruction is obtained with 500 iterations of the difference-map (DM) algorithm [23] and the illumination function retrieved at this point is shown in Fig. 2.

After the DM reconstructions, approximately 15% of the reconstructions exhibit phase vortices, which are singularities in the phase part of a two-dimensional (2D) complex

FIG. 4. The numerical curl of the phase map shown in Fig. 3, as computed with Eq. (1).

field [24]. An example of a phase reconstruction affected by vortices is shown in Fig. 3.

These reconstructions are corrected using an automatic phase-vortex detection and cancellation algorithm ("VortRem"), described in the following.

Locating phase vortices amounts to identifying the points at which the curl of the phase gradient (modulo 2π) is nonzero. With the phase defined on a 2D grid, a vortex is found at position $(i + 1/2, j + 1/2)$ if the numerical curl,

$$\nabla \times [\nabla\phi]_{2\pi} = [\phi_{i+1,j} - \phi_{i,j}]_{2\pi} + [\phi_{i+1,j+1} - \phi_{i+1,j}]_{2\pi} \\ + [\phi_{i,j+1} - \phi_{i+1,j+1}]_{2\pi} + [\phi_{i,j} - \phi_{i,j+1}]_{2\pi},$$
(1)

is nonzero. Here, $[\phi]_{2\pi} = (\phi + \pi \pmod{2\pi}) - \pi$ keeps the phase wrapped in the interval $(-\pi, \pi]$. Normally, the curl is zero at all but just a few points, where the values are $\pm 2\pi$, corresponding to negative or positive topological charges.

Figure 4 shows the curl of the phase map from Fig. 3. For the complete data set, we find that phase maps contain
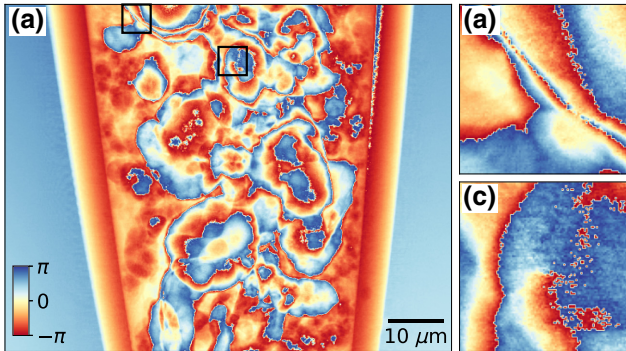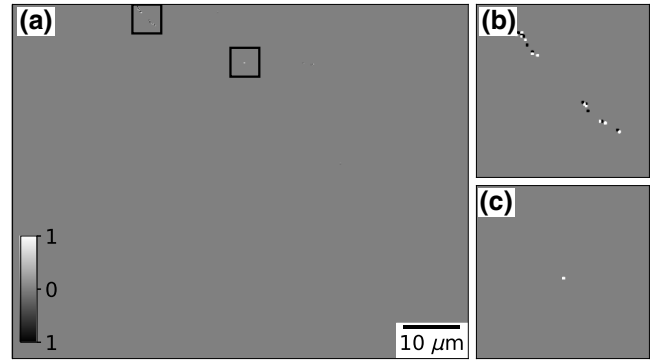

FIG. 3. (a) The phase part of the transmission function of the sample after 500 iterations of the DM algorithm. (b),(c) Enlargements of areas containing vortices.
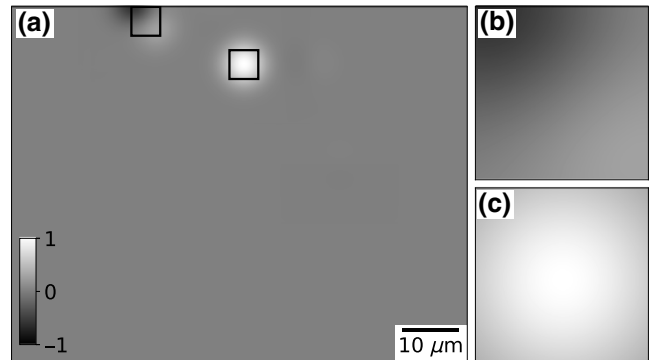

FIG. 5. The low-pass filtered version of the numerical curl. Neighboring vortices of opposite charge are seen to mostly cancel each other, so that after thresholding, a single vortex, centered in (c), is left to be corrected.
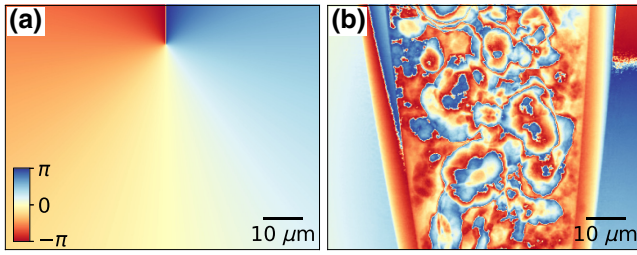
FIG. 6.   Vortex cancellation using a naive antivortex (a) produces strong gradients in the areas known to be uniform (b).
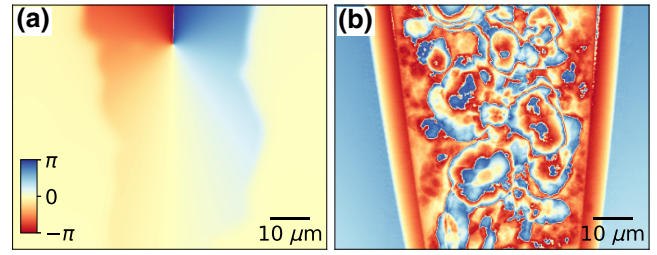

FIG. 7.   (a) An antivortex map corrected using the absorption part of the reconstruction. (b) No global gradient or offset is introduced in the highly transmissive area of the sample.

many dozens of vortices. However, most of them are seen to be part of close vortex-antivortex pairs located along sharp edges in the sample, where sudden phase jumps are common. Although they are artifacts, these vortices are found to cause few difficulties in the data-processing pipeline.

A low-pass filter applied on the numerical curl (see Fig. 5) is used to artificially merge vortex pairs and, through proper thresholding, detect only vortices that are isolated at the scale set by the filter (50 pixels in our analysis).

Given the list of relevant vortices, cancellation merely amounts to multiplying each vortex with a synthetic vortex of opposite charge. When vortices are far from each other or when the total charge of the image is nonzero, this cancellation operation can lead to spurious phase gradients and offsets in the reconstruction. This effect can be seen in Fig. 6. While these nonphysical gradients can be corrected by running further iterations of the ptychographic reconstruction algorithm, we devise a heuristic to reduce their impact, by forcing the cancellation phase to concentrate the gradient in regions where transmission is lower, as shown in Fig. 7.

To allow the reconstruction to adjust back to the data model after the nonphysical phase gradients introduced by

the VortRem algorithm, 500 more DM iterations are performed. This step is followed by 1000 iterations of the maximum-likelihood (ML) algorithm [25], which is found to improve the quality of the reconstruction substantially.

Any phase ramp that may have accumulated is then removed via a bilinear fit of the background region for each of the reconstructed projections. The phase is then unwrapped, using a quality map method [26], and the projections realigned for the sample shift that occurs during the full tomographic scan. Only a drift in the vertical direction is detected via image registration of an amount of approximately 10 pixels.

The tomographic reconstruction is performed from the phase projections using the filtered-back-projection algorithm.

The quantity reconstructed in the phase tomogram is the real part of the refractive-index decrement δ, which, at the photon energy used, is proportional to the electron density ρ_e. The mass density ρ of the specimen can be calculated from this electron density [27]:

$$\rho = \frac{A}{Z}\frac{1}{N_A} \times \rho_e = \frac{A}{Z}\frac{1}{N_A} \times \delta\frac{2\pi}{\lambda^2 r_0}, \qquad (2)$$
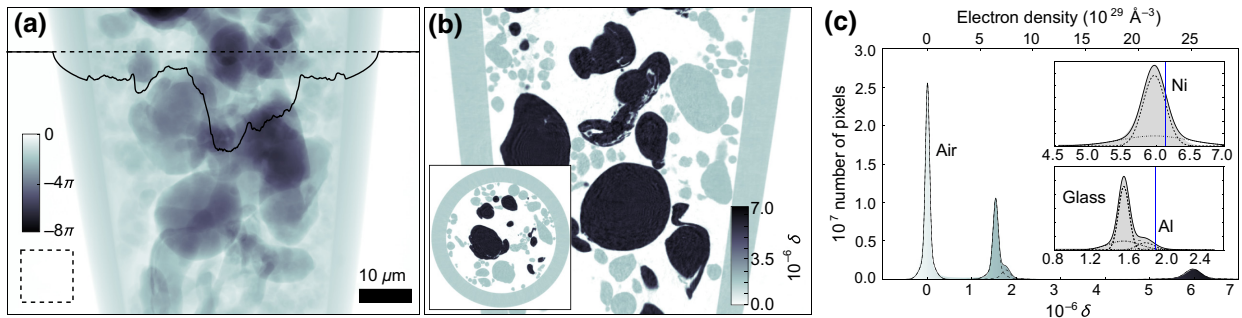

FIG. 8.   (a) The phase projection of Al and Ni particles in a capillary obtained with the near-field ptychographic and VortRem algorithms. The profile taken along the dashed line can be seen superimposed on the figure. The dashed-square area at the bottom left of the image is used to determine the phase sensitivity. (b) A sagittal slice of the reconstructed value, with an axial slice through the same volume as an inset. The scale bar in (a) and (b) is the same. (c) A combined histogram of the density values measured in the full volume. The result of the fit of the histogram peaks with squared-Lorentzian functions is used to determine the refractive-index and mass-density values of the materials of the sample. The blue vertical lines represent the tabulated values for pure materials.

where A is the molar mass and Z is the number of electrons in the molecule. N_A is the Avogadro number, λ is the wavelength of the x rays, and r_0 is the classical electron radius. The ratio A/Z is 2.10 for Ni and 2.08 for Al.

IV. RESULTS

The final phase projection in Fig. 8(a) shows the edges of the glass capillary, the smaller Al particles, and the denser Ni particles. The maximum phase shift measured in this projection is 26.3 rad and the standard deviation is 8×10^{-3}, as calculated in the region of 200×200 pixels indicated by the dashed square in Fig. 8(a). From these values, we conclude that the contrast-to-noise ratio (CNR)—in other words, the effective dynamic range—is above 3000, as illustrated by the profile plot in Fig. 8(a).

A sagittal slice through the reconstructed phase tomogram is shown in Fig. 8(b), with an axial slice from the same volume as an inset. The density resolution is measured in a volume of $100 \times 100 \times 100$ pixels in the background (air) and gives a value of 4.5×10^{-8} for δ, corresponding to 0.06 g/cm^3 [28]. Figure 8(c) shows the histogram of the electron density of the full volume, where the peaks represent the different materials forming the sample. All peaks are found to match a squared-Lorentzian curve well. The values for the center and standard deviation of each peak are extracted from these fits.

The comparison of the histogram-based values with the theoretical values for pure elements extracted from the NIST database [29] are compiled in Table I. While the particles might have impurities or be partly in an oxidation state, we compare our results with the theoretical

TABLE I. A comparison of the refractive-index decrements δ and densities ρ extracted from the histogram of the whole volume, compared with tabulated data (NIST database). The errors on the measured values are the standard deviations derived from the fitted width of each peak.

	δ ($\times 10^{-6}$)		ρ (g/cm^3)	
	Measured	Theory	Measured	Theory
Al	1.78 ± 0.08	1.87	2.58 ± 0.12	2.70
Ni	5.97 ± 0.17	6.14	8.75 ± 0.26	8.91

values for pure materials to provide an upper limit to the underestimation from near-field ptychography. An underestimation of the refractive-index measurements, by 4.8% and 2.8% for Al and Ni, respectively, can be observed. The measured density of the borosilicate pipette is 2.15 ± 0.08 g/cm^3, underestimated by 3.5% with respect to the nominal value of 2.23 ± 0.02 g/cm^3. The underestimation will be discussed further below.

The spatial resolution for this measurement is estimated using the edge-spread function from the edge of the container in the axial slices shown in the inset of Fig. 8(b). The width of the edge-spread function of 1.86 pixels, corresponding to 94.3 nm, can be taken as an estimation of the 3D spatial resolution of our data.

Due to the high quality of the density volume, segmentation of the microparticles in the sample is straightforward. Both Al and Ni particles are found through thresholding of the volume inside the capillary. Particles are then labeled using a watershed segmentation of the distance transform.
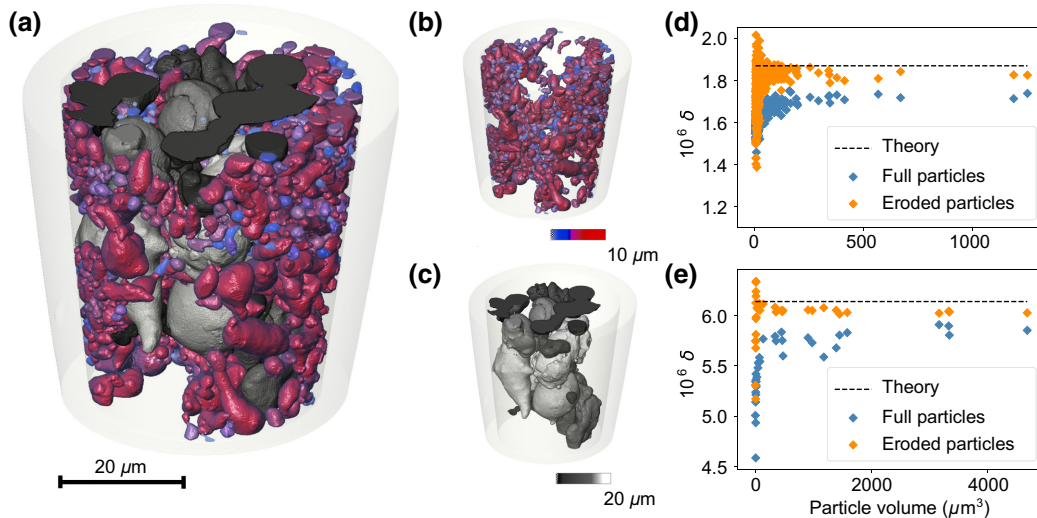

FIG. 9. (a)–(c) Segmentation of the microparticles, color coded according to their size, measured here by means of the equivalent diameter. The top row [i.e., panels (b) and (d)] shows the rendering and measurements of the Al particles, while the bottom row [i.e., panels (c) and (e)] shows the corresponding data for the Ni particles. (d),(e) Scatter plots illustrating the values of the δ measurements of the segmented particles as a function of their volume. The measurements for the full particles are plotted with blue diamonds, while the measurements for the same particles where 10 pixels have been removed from their edges are plotted with orange diamonds.

Neighboring domains sharing a large fraction of their surface are subsequently merged. Segmentation and labeling are conducted on a volume downsampled by a factor of 2 to increase the computing speed and reduce the memory requirements. Figures 9(a)–9(c) show the results of the segmentation, in which the particles are color coded according to their material and size. These renderings allow visualization of the particle size distribution within the glass capillary and show that many particles are far from their nominal spherical shape.

The segmentation is used to evaluate the effects of the size of the particles on the measurements of their refractive index. A total of 34 Ni particles and 554 Al particles are considered in this study, with an average volume of 727.0 μm^3 and 36.8 μm^3 for Ni and Al, respectively. The scatter plots of Figs. 9(d) and 9(e) display the average δ values of each of these particles as a function of their volume (blue diamonds). Not surprisingly, the density of the smaller particles shows a stronger scatter than for the larger ones. Yet δ is systematically underestimated even for large particles. The agreement with the tabulated values improves dramatically when all particles are eroded (i.e., a 10-voxel-thick shell is removed from their segmented volume). The resulting δ values are shown in Fig. 9 as orange diamonds. The largest four Al and Ni particles give, after erosion, an average value for δ of 1.82×10^{-6} and 6.03×10^{-6}, respectively, reducing the underestimation to 2.3% (Al) and 1.7% (Ni) and indicating that the density decreases closer to interfaces. The precise origin of this effect is currently unknown. A physical origin is possible, since the density of an object is most prone to differ from its pure-material value at the interface—because of oxidation, for instance. However, reconstruction artifacts are also more likely to appear along sharp edges, because the broad spectrum of spatial frequencies required to represent a sharp edge can be affected by various experimental limitations, leading to a loss of signal.

V. DISCUSSION AND CONCLUSIONS

Near-field ptychography allows high-sensitivity measurements of the refractive index and mass density of microstructures in the investigated sample and also when the features have a large difference in refractive index [30], which might be a challenging condition for other holographic techniques. Even though it cannot be directly compared because of the difference in dose used in the two measurements, we note that the δ sensitivity of this experiment evaluated as 4.5×10^{-8} is one order of magnitude smaller than that obtained with far-field ptychography with a similar pixel size [6].

The underestimation of δ observed for Al is 5.3% from the histogram but decreases to 2.3% when considering only the bulk of the material, while the underestimation for Ni

is around 2% with both analysis methods. The highest discrepancy for Al is partly due to the fact that the Al particles are smaller in size and we find that the refractive-index measurements become more accurate for larger features. Our results are comparable with those obtained by Diaz *et al.* [6], who have reported an underestimation of 2% for the refractive index measured in a volume of interest in the bulk of a SiO_2 sphere.

For near-field ptychography, the underestimation might be due to a combination of effects including partial coherence of the x-ray beam and an imperfect theoretical estimation of the point-spread function of the detector. These might be improved by using a more sophisticated reconstruction [31].

The spatial resolution in three-dimensions, here of approximately 2 pixels, can be tuned depending on the experimental needs by changing the geometry of the setup and the effective pixel size at the sample plane and is ultimately limited by the size of the x-ray source.

Our phase-vortex-removal algorithm (VortRem) described in this work may be of benefit for future phase-contrast experiments that are prone to this type of artifact, especially when features with high density differences are present in the investigated sample.

These results may be fundamental for the application of near-field ptychography and the interpretation of the quantitative data provided by this technique in its future extensive use at high-brilliance sources for a large variety of applications.

[1] E. Biermans, L. Molina, K. J. Batenburg, S. Bals, and G. Van Tendeloo, Measuring porosity at the nanoscale by quantitative electron tomography, Nano Lett. **10**, 12 (2010).

[2] D. Huang, E. A. Swanson, C. P. Lin, J. S. Schuman, W. G. Stinson, W. Chang, M. R. Hee, T. Flotte, K. Gregory, and C.

A. Puliafito *et al.*, Optical coherence tomography, Science **254**, 5035 (1991).

[3] M. A. Le-Gross, G. McDermott, and C. A. Larabell, X-ray tomography of whole cells, Curr. Opin. Struct. Biol. **15**, 5 (2005).

[4] C. Holzner, M. Feser, S. Vogt, B. Hornberger, S. B. Baines, and C. Jacobsen, Zernike phase contrast in scanning microscopy with X-rays, Nat. Phys. **6**, 883 (2010).

[5] M. Dierolf, A. Menzel, P. Thibault, P. Schneider, C. M. Kewish, R. Wepf, O. Bunk, and F. Pfeiffer, Ptychographic X-ray computed tomography at the nanoscale, Nature **467**, 7314 (2010).

[6] A. Diaz, P. Trtik, M. Guizar-Sicairos, A. Menzel, P. Thibault, and O. Bunk, Quantitative x-ray phase nanotomography, Phys. Rev. B **85**, 2 (2012).

[7] F. Pfeiffer, X-ray ptychography, Nat. Photonics **12**, 9 (2018).

[8] I. Zanette, B. Enders, M. Dierolf, P. Thibault, R. Gradl, A. Diaz, M. Guizar-Sicairos, A. Menzel, F. Pfeiffer, and P. Zaslansky, Ptychographic X-ray nanotomography quantifies mineral distributions in human dentine, Sci. Rep. **5**, 9210 (2015).

[9] M. Holler, M. Guizar-Sicairos, E. H. R. Tsai, R. Dinapoli, E. Müller, O. Bunk, J. Raabe, and G. Aeppli, High-resolution non-destructive three-dimensional imaging of integrated circuits, Nature **543**, 402 (2017).

[10] W. Szmyt, S. Vogel, A. Diaz, M. Holler, J. Gobrecht, M. Calame, and C. Dransfeld, Protective effect of ultra-thin alumina film against diffusion of iron into carbon fiber during growth of carbon nanotubes for hierarchical composites investigated by ptychographic X-ray computed tomography, Carbon **115**, 347 (2017).

[11] P. Cloetens, W. Ludwig, and J. Baruchel, Holotomography: Quantitative phase tomography with micrometer resolution using hard synchrotron radiation x rays, Appl. Phys. Lett. **75**, 2912 (1999).

[12] M. Töpperwien, F. van der Meer, C. Stadelmann, and T. Saldilt, Three-dimensional virtual histology of human cerebellum by X-ray phase-contrast tomography, Proc. Natl. Acad. Sci. **115**, 27 (2018).

[13] Y. Yang, R. Xu, K. Zhang, S. J. Lee, L. Mu, P. Liu, C. K. Waters, S. Spence, Z. Xu, and C. Wei *et al.*, Quantification of heterogeneous degradation in Li-ion batteries, Adv. Energy Mater. **9**, 25 (2019).

[14] M. Langer, A. Pacureanu, H. Suhonen, Q. Grimal, P. Cloetens, and F. Peyrin, X-ray phase nanotomography resolves the 3D human bone ultrastructure, PLOS ONE **7**, 8 (2012).

[15] M. Stockmar, P. Cloetens, I. Zanette, B. Enders, M. Dierolf, F. Pfeiffer, and P. Thibault, Near-field ptychography: Phase retrieval for inline holography using a structured illumination, Sci. Rep. **3**, 1927 (2013).

[16] A. L. Robisch, K. Kröger, A. Rack, and T. Saldilt, Near-field ptychography using lateral and longitudinal shifts, New J. Phys. **17**, 7 (2015).

[17] M. Stockmar, I. Zanette, M. Dierolf, B. Enders, R. Clare, F. Pfeiffer, P. Cloetens, A. Bonnin, and P. Thibault, X-Ray Near-Field Ptychography for Optically Thick Specimens, Phys. Rev. Appl. **3**, 014005 (2015).

[18] M. Stockmar, M. Hubert, M. Dierolf, B. Enders, R. Clare, S. Allner, A. Fehringer, I. Zanette, J. Villanova, and J. Laurencin *et al.*, X-ray nanotomography using near-field ptychography, Opt. Express **23**, 10 (2015).

[19] J. Gussone, K. Bugelnig, P. Barriobero-Vila, J. Cesar da Silva, U. Hecht, C. Dresbach, F. Sket, P. Cloetens, A. Stark, and N. Schell *et al.*, Ultrafine eutectic Ti-Fe-based alloys processed by additive manufacturing—A new candidate for high temperature applications, Appl. Mar. Today **20**, 100767 (2020).

[20] www.goodfellow.com.

[21] R. Clare, M. Stockmar, M. Dierolf, I. Zanette, and F. Pfeiffer, Characterization of near-field ptychography, Opt. Express **23**, 15 (2015).

[22] B. Enders and P. Thibault, A computational framework for ptychographic reconstructions, Proc. Math. Phys. Eng. Sci. **472**, 2196 (2016).

[23] P. Thibault, M. Dierolf, A. Menzel, O. Bunk, C. David, and F. Pfeiffer, High-resolution scanning X-ray diffraction microscopy, Science **321**, 5887 (2008).

[24] D. Paganin, *Coherent X-Ray Optics*, Oxford Series on Synchrotron Radiation (Oxford University Press, New York, 2006).

[25] P. Thibault and M. Guizar-Sicairos, Maximum-likelihood refinement for coherent diffractive imaging, New J. Phys. **14**, 6 (2012).

[26] D. Ghiglia and M. Pritt, *Two-Dimensional Phase Unwrapping: Theory, Algorithms, and Software* (Wiley, New York, 1998).

[27] A. Guinier, *X-Ray Diffraction in Crystals, Imperfect Crystals, and Amorphous Bodies* (Dover, Minneola, NY, 1994).

[28] The Guinier approximation ($A/Z = 2$) is used for the conversion of the standard deviation of δ to mass density.

[29] V. K. Shen *et al.*, NIST Standard Reference Simulation Website, NIST Standard Reference Database No. 173, (NIST, Gaithersburg, MD) 20899 (retrieved July 2019).

[30] Note that while in this paper we report a detailed study on the real part of the refractive index δ, in principle near-field ptychography also gives access to the imaginary part β related to the absorption of the x rays. Algorithmic refinements or further technique developments hold the potential to provide, in the future, absorption data of sufficient quality to allow complementary material characterization using the β information.

[31] P. Thibault and A. Menzel, Reconstructing state mixtures from diffraction measurements, Nature **494**, 68 (2013).